How impedance measurements and imaging can be used to characterize the conductivity of tissues during the workflow of an electroporation-based therapy

Olivier Sutter, Damien Voyer, Jean-Pierre Tasu, Clair Poignard

How impedance measurements and imaging can be used to characterize the conductivity of tissues during the workflow of an electroporation-based therapy

O. Sutter, D. Voyer, J.-P. Tasu and C. Poignard

Abstract — **In this paper we investigate the possibility of using needles, which the interventional radiologist inserts near a deep-seated tumor during an electroporation-based therapy, to characterize the electrical conductivity of patient's tissues. Specifically, we propose to exploit voltage/current measurements and imaging that are performed prior to the application of electroporation pulses. The approach is partly based on the concepts of electrical impedance tomography; however, imaging is used to build a specific geometric model and compensate for the lack of information resulting from the small number of electrodes available. 3D canonical and clinical examples, where a few electrodes surround a tumor, demonstrate the feasibility of this method: solving the inverse problem to estimate tissues conductivity converges in a few iterations. For a given error on the measurement, it is also possible to calculate the error on the estimated conductivities. The uncertainty error with clinical data is at best 5% for one of the tissues identified, due to the limitations of the clinical device used. Various improvements to clinical devices are discussed to make the conductivity estimation more accurate but also to extract more information.**

Index Terms — **DC electrical conductivity, Electrical Impedance Tomography, Electroporation**

I. Introduction

THESE last years, electroporation-based therapies – either irreversible electroporation (IRE) or electrochemotherapy – are booming and are the subject of a growing number of clinical trials to treat malignant tumors [1-5]. These therapies provide interesting alternatives to standard non-surgical ablative techniques – radiation therapy and radiofrequency ablation – for treating deep-seated non resectable tumors. Unlike conventional ablative techniques, which are based on thermal diffusion and mainly use a single needle, electroporation ablation is based on cell permeabilization thanks to the electric field induced by several needles. Numerous needles (at least 3 but often 5 to 6) have to be judiciously placed close to the deep-seated tumor to generate the electric field that will destroy the cancer cells. In order to assist interventionists, numerical tools have been developed to compute the distribution of the electric field [6, 7]. In these computations, needle placement is fixed a priori to ensure optimal treatment efficacy. But in the case of deep-seated tumors, the percutaneous needle placement comes up against the problem of anatomical constraints. In the clinical setting of an IRE procedure, interventional radiologists place needles as best as they can under imaging guidance [8]. As a result, the theoretical placement configuration is often unfeasible for hepatic or pancreatic tumors located close to vital structures. In order to build a realistic model including tumor and needles, the authors in [9] proposed a numerical process implemented in parallel with the clinical workflow. As shown in [10], the precise localization of the needles is crucial for accurate computation of electric field distribution. The geometric model is built up from imaging carried out during the IRE procedure (to recover the exact coordinates of the needles) and from other imaging carried out at the beginning or a few days before the intervention (to obtain the localization of the target tumor). Next, the electric field distribution is computed from a nonlinear model of DC electrical conductivity, where the electroporation phenomenon is described by a sigmoid. By visualizing the simulated electric field before the electroporation pulses are applied, the clinician can assess whether or not coverage of the tumor will be sufficient. He can then decide to replace or add an electrode before starting the IRE pulses. Ultimately, the clinician will also be able to optimize treatment by adjusting the parameters of the generator (voltages applied, number of pulses, etc.).

However, it is necessary to know the electric conductivity of the different tissues identified in the model, in order to accurately compute the electric field before, during or after the electroporation process [11, 12]. The literature provides a database of the electric properties of healthy tissues [13, 14]. But these data give a mean value, whereas electrical properties vary greatly from one individual to another when measurements are carried out in vivo, as reported for example in [13]. Magnetic resonance imaging (MRI) could be used to compute a patient's impedance imaging, but DC conductivity extraction is only possible by injecting an external DC current into the patient's body [15]. Another possibility is to use impedance measurements: 4-electrodes systems have already been used to monitor low frequency conductivity during the electroporation process [16] or to estimate the size of IRE ablation [17]. The conductivity measured is that of the targeted tissue, provided the electrodes are fully immersed in homogeneous tissue. Otherwise, this conductivity is the equivalent conductivity of the entire biological system. To differentiate conductivity in different parts of the system, other electrodes have to be added: electrical impedance tomography (EIT) consists precisely in using an array of electrodes to build an image of the conductivity distribution around the sensor. EIT experiments have already been carried out in laboratory to monitor the extent of the electroporated area [18]. The drawback of EIT is that a large number of

electrodes are required to achieve a good resolution (16 to 32 electrodes in a conventional EIT sensor) and the device cannot be used to investigate an area deep inside the patient's body [19].

In this article, we propose to accurately estimate the DC electrical conductivity of biological tissues specific to the patient being treated with IRE, in order to calibrate electroporation models. We investigate a technique that combines imaging performed during the workflow of electroporation-based therapy with impedance measurements that can be performed using the needles inserted near the deep-seated tumor. Imaging provides a realistic geometric model with the different tissues and their real shape, while impedance measurements are exploited to estimate the electrical properties of these tissues. This technique can be considered as a degraded EIT where only a few electrodes are available; but this drawback is compensated by the information provided by imaging. In section II, the theoretical formulation of the problem is presented based on well-known concepts in EIT; the propagation of measurement uncertainty is also analyzed to quantify the error on the estimated conductivities. In section III, we demonstrate the feasibility of the method with 3D numerical simulations, first in a canonical case and then in a clinical case with real data.

II. Theory

A. *Formulation of the forward problem*

We consider the case where six electrodes are inserted in the vicinity of a deep-seated tumor in order to apply electroporation voltage pulses (see Figure 1).

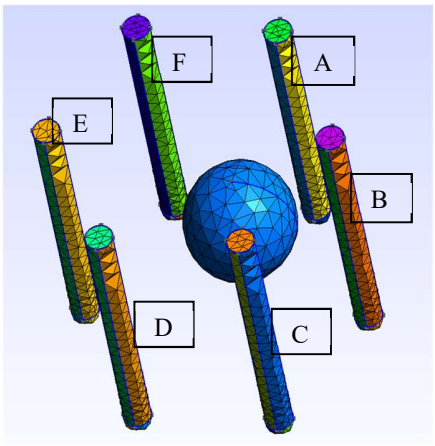

Fig. 1. 3D model of six electrodes that surround a tumor.

Impedance measurement can be performed using the same electrodes in order to characterize the conductivity of tissues in the tumor vicinity. To do this, electrode pairs need to be defined in a similar way as in EIT: there are different ways of selecting electrode combinations [20, 21]. Here, we assign an index between 1 and 6 for the six electrode pairs defined with the neighboring method (see Table 1).

TABLE I
SELECTION OF ELECTRODE PAIRS WITH THE NEIGHBORING METHOD.

Pair index	First electrode	Second electrode
1	A	B
2	B	C
3	C	D
4	D	E
5	E	F
6	F	A

Then, a set of impedance measurements is carried out. For a given electrode pair, denoted *j,* a DC current I_j is injected in the first electrode and collected in the second. Next, a potential difference ΔV_{ij} is measured between the electrodes of another electrode pair, denoted *i*, and the impedance Z_{ij} is computed as follows:

$$Z_{ij}=\Delta V_{ij}/I_j \tag{1}$$

From an electromagnetic point of view, the expression of the impedance Z_{ij} can be written as follows:

$$Z_{ij} = \frac{1}{I_i\, I_j} \iiint_{\Omega} \sigma\, \nabla\phi_i\, \nabla\phi_j\, d\Omega \tag{2}$$

where ϕ_m is solution of the following electrokinetic problem:

$$\text{Problem } m \begin{cases} \nabla . (\sigma\, \nabla\phi_m) = 0 \;\; in \;\; \Omega \\ \phi_m|_{\Gamma_{m+}} = +V \\ \phi_m|_{\Gamma_{m-}} = -V \\ \\ \phi_m|_{\Gamma_p} = V_p \;\; with \iint\limits_{\Gamma_p} \sigma \frac{\partial \phi_m}{\partial n} d\Gamma = 0 \\ \\ p = \{1, 2, \cdots, 6\} \setminus \{m_+, m_-\} \\ \sigma \frac{\partial \phi_m}{\partial n} = 0 \;\; on \;\; \partial\Omega \setminus \{\Gamma_1, \cdots, \Gamma_6\} \end{cases} \tag{3}$$

with σ the conductivity defined in the computational domain Ω, Γ_p the bounded surface of electrode $p = \{1, \ldots, 6\}$. Indexes m_+ and m_- are relative to the electrodes of pair denoted m, into which the current I_m is respectively injected and collected. The other electrodes are modelled as perfect conductors with an unknown floating potential V_p for $p = \{1, \ldots, 6\} \setminus \{m_+, m_-\}$ to compute. The current I_m is given by:

$$I_m = \iint\limits_{\Gamma_{m+}} \sigma \frac{\partial \phi_m}{\partial n} d\Gamma = \frac{1}{2V} \iiint_{\Omega} \sigma\, |\nabla\phi_m|^2 \;\; d\Omega \tag{4}$$

Calculating Z_{ij} from (2) therefore involves solving two problems (3). In the first problem ($m = i$), a potential difference equal to $2V$ is applied between the two electrodes of pair i; the current I_i flowing through these two electrodes is deduced by calculating (4). In the second problem ($m = j$), a potential difference of $2V$ is applied between the two electrodes of pair j; from (4) we deduce the current I_j flowing through these two electrodes.

We are interested with the inverse problem of determining the conductivity distribution σ within the sample from impedance measurements.

In practice, voltage drops are observed at electrode/tissue interfaces where low amplitude currents flow. This is why impedances are not taken into account in EIT analysis when voltage measurement uses an electrode where the current flows. Unfortunately, the devices used in IRE clinical trials, such as the Nanoknife (AngioDynamics, USA), only measure the voltage difference between the electrodes where the current flows. However, the current amplitude is high compared to the signals used in EIT. Under these conditions, there is no voltage drop due to interfacial phenomena (see appendix for details). As a result, voltage measurement can be carried out using an electrode where a high amplitude current flows.

In the theoretical section that follows, we have chosen to formulate the problem according to the set of impedances that an EIT device would provide. However the problem is formally the same for an IRE device that would provide only self-impedances (i.e. Z_{ii}). We have discussed this latter case with clinical data in section III.B.

Following the restrictions defined in EIT, only nine measurements can be used in our problem: Z_{13}, Z_{14}, Z_{15}, Z_{24}, Z_{25}, Z_{26}, Z_{35}, Z_{36} and Z_{46}. As we have very few measurements, we will take advantage of the information provided by imaging to solve the inverse problem.

B. Traditional EIT approach

Consider the problem where imaging leads to a geometric model with a tumor surrounded by a single healthy tissue. For a given conductivity distribution σ in the whole domain, the difference ΔZ_{ij} between measured and modelled impedances can be approximated at the first order from Geselowitz's theorem [22, 23]:

$$\Delta Z_{ij}(\sigma) \approx \frac{-1}{I_i\, I_j} \iiint_{\Omega} \Delta\sigma\, \nabla\phi_i(\sigma)\, \nabla\phi_j(\sigma) d\Omega \tag{5}$$

where $\Delta\sigma$ is the difference between real and modelled conductivity distributions.

Numerically, the domain Ω is discretized into K elements Ω_k where the conductivity is assumed constant. Then,

$$\Delta Z_{ij}(\sigma) = \sum_{k=1}^{K} S_{ijk}(\sigma)\ \Delta\sigma_k \tag{6}$$

with $\Omega = \bigcup_k \Omega_k$, $\Delta\sigma = \Delta\sigma_k$ in Ω_k and the sensitivity terms $S_{ijk}(\sigma) = \frac{-1}{I_i\, I_j} \iiint_{\Omega_k} \nabla\phi_i(\sigma)\ \nabla\phi_j(\sigma)\ d\Omega$

Using the nine measurements, the resulting problem to solve can be put into matrix form:

$$[\boldsymbol{\Delta Z}(\sigma)] = [\boldsymbol{S}(\sigma)][\boldsymbol{\Delta\sigma}] \tag{7}$$

with $[\boldsymbol{\Delta Z}(\sigma)] = [\Delta Z_{13}(\sigma)\ , \Delta\ Z_{14}(\sigma)\ , \cdots , Z_{46}(\sigma)]^t$, the sensitivity matrix $[\boldsymbol{S}(\sigma)] = \begin{bmatrix} S_{131}(\sigma) & S_{132}(\sigma) & \cdots & S_{13\ }(\sigma) \\ S_{141}(\sigma) & S_{142}(\sigma) & \cdots & S_{14K}(\sigma) \\ & \vdots & & \\ S_{461}(\sigma) & S_{462}(\sigma) & \cdots & S_{46K}(\sigma) \end{bmatrix}$ and $[\boldsymbol{\Delta\sigma}] = [\Delta\sigma_1\ , \Delta\sigma_2, \cdots , \Delta\sigma_K]^t$.

The problem is ill-posed since we have only nine measurements and the conductivity has to be estimated over a large number of elements K. A penalty term can be added to regularize the problem:

$$\underset{[\boldsymbol{\Delta\sigma}]}{Argmin}\{\|[\boldsymbol{\Delta Z}] - [\boldsymbol{S}]\ [\boldsymbol{\Delta\sigma}]\|^2 + \alpha P([\boldsymbol{\Delta\sigma}])\} \tag{8}$$

where P is the regularisation term and α a parameter to choose. There are many ways to set the penalty term P, including Tikhonov regularization [24], L1 norm or Total Variation denoising [25].

Despite this improvement, the conductivity distribution will not be accurately estimated in our problem, due to the limited number of measurements. On the other hand, we have prior information on the tumor localization from imaging. We propose to re-examine the problem by adding the hypothesis that the conductivity of tumor and healthy tissue is assumed to be constant. With this assumption, there are only two unknowns, which greatly facilitates the numerical resolution of the nonlinear problem.

C. Problem where the conductivity is assumed to be constant

In this case, there are only two sensitivity terms for a given impedance measurement:

$$S_{ij\ d}(\sigma) = \frac{-1}{I_i\ I_j} \iiint_{\Omega_d} \nabla\phi_i(\sigma)\ \nabla\phi_j(\sigma) d\Omega \tag{9}$$

where d refers to the domain under consideration (healthy tissue or tumor).

The sensitivity matrix is reduced to a 9×2 matrix:

$$[\boldsymbol{S}(\sigma)] = \begin{bmatrix} S_{13\ tissue}\ (\sigma) & S_{13\ tumor}(\sigma) \\ S_{14\ tissue}\ (\sigma) & S_{14\ tumor}\ (\sigma) \\ \vdots & \vdots \\ S_{46\ \ tissue}\ (\sigma) & S_{46\ \ tumor}\ (\sigma) \end{bmatrix} \tag{10}$$

and it is no longer necessary to introduce a regularization term into the minimization problem (8). The minimization problem with $\alpha = 0$ is quadratic and we can derive a linear system to compute the incremental conductivity distribution $\Delta\sigma$:

$$[\boldsymbol{\Delta\sigma}] = ([\boldsymbol{S}(\sigma)]^t[\boldsymbol{S}(\sigma)])^{-1}([\boldsymbol{S}(\sigma)]^t[\boldsymbol{\Delta Z}(\sigma)]) \tag{11}$$

As the initial problem (5) is nonlinear, the conductivity distribution σ is computed iteratively starting from an initial guess (see Algorithm I). The initial conductivity σ_0 for a given domain is chosen to be equal to the expected tissue conductivity.

ALGORITHM I
SOLUTION PROPOSED IN SECTION II.C

$\sigma_{tissue} = \sigma_0$ and $\sigma_{tumor} = \sigma_0$
error = 1
while error > threshold
  for m = 1, …, 6
    Solve Problem m
  for i-j = 1-3, 1-4 , …, 4-6
    Compute $S_{ij\ tissue}$ and $S_{ij\ tumor}$
    Compute ΔZ_{ij}
  $[\boldsymbol{\Delta\sigma}] = ([\boldsymbol{S}]^t[\boldsymbol{S}])^{-1}([\boldsymbol{S}]^t[\boldsymbol{\Delta Z}])$
  $\sigma_{tissue} \leftarrow \sigma_{tissue} + [\boldsymbol{\Delta\sigma}][1]$
  $\sigma_{tumor} \leftarrow \sigma_{tumor} + [\boldsymbol{\Delta\sigma}][2]$
  error = $\|[\boldsymbol{\Delta Z}]\|^2$

The computation of the sensitivity terms can also be used to analyze the propagation of uncertainties when solving the inverse problem. The question is how an error on impedance measurement translates into estimated conductivities.

To answer this question, we can consider the measured impedances as independent random variables with a given variance. The variance on the estimated conductivity for healthy tissue or tumor is then given by:

$$VAR(\sigma_d) = [\boldsymbol{J_d}]^t \begin{bmatrix} VAR(Z_{13}) & 0 & \cdots & 0 \\ 0 & VAR(Z_{14}) & & \\ \vdots & & \ddots & \\ 0 & & & VAR(Z_{46}) \end{bmatrix} [\boldsymbol{J_d}] \tag{12}$$

with VAR the variance and $[\boldsymbol{J_d}]$ the Jacobian defined as $[\boldsymbol{J_d}] = \begin{bmatrix} \partial\sigma_d/\partial Z_{13} \\ \partial\sigma_d/\partial Z_{14} \\ \vdots \\ \partial\sigma_d/\partial Z_{46} \end{bmatrix}$.

The Jacobian terms can be extracted from (11). Specifically, the Jacobian terms for tissue and tumor with respect to the ith measurement are given by:

$$\begin{bmatrix} [\boldsymbol{J_{tissue}}][i] \\ [\boldsymbol{J_{tumor}}][i] \end{bmatrix} = ([\boldsymbol{S}(\sigma)]^t[\boldsymbol{S}(\sigma)])^{-1}([\boldsymbol{S}(\sigma)]^t[\boldsymbol{\delta_i}]) \tag{13}$$

with $[\boldsymbol{\delta_i}][i] = 1$ and $[\boldsymbol{\delta_i}][j] = 0$ for $j \neq i$.

III. SIMULATION RESULTS

A. 3D canonical case

We consider the 3D geometrical problem where six regularly spaced electrodes surround a tumor as shown in Figure 1. The length of the electrodes is 9 mm; the tumor is perfectly spherical with a radius of 2 mm and is slightly eccentric.

Numerical experiments were performed for a tumor conductivity σ_{tumor} = 2.0 σ_{tissue} where the tissue conductivity σ_{tissue} = 0.1 S/m. Problem (3) was solved for m = {1, 2, …, 6} using finite element method implemented with Freefem++ [26]. To avoid "inverse crime" [27, 28], we used two different meshes (with 76 408 elements for the forward problem and 48 794 for the inverse problem; see supplementary files 1).

The convergence study reported in Table II shows that Algorithm I converges after 4 iterations with a relative error on the estimated conductivities lower than 1%. Convergence is achieved more quickly for the tissue, because the initial guess was closer to the true value compared with the tumor.

TABLE II
CONVERGENCE STUDY FOR THE CANONICAL CASE.
σ_{tissue} = 0.1 S/m, σ_{tumor} = 0.2 S/m and σ_0 = 0.05 S/m.

Iteration	Error on σ_{tissue}	Error on σ_{tumor}
1	25.0 %	53.6 %
2	6.2 %	25.1 %
3	0.3 %	4.6 %
4	0.1 %	0.5 %
5	0.1 %	0.9 %
6	0.1 %	0.9 %
7	0.1 %	0.9 %

Table III reports the relative change of impedance with and without tumor in this numerical problem. The variation is not greater than 5% for all the possible measurements. Under these conditions, the estimation may be altered by measurement error. The uncertainty on the estimated conductivities can be predicted using the variance analysis presented in section II.C. Here we consider that the standard deviation ($\sqrt{VAR}$) for the different impedance Z_{ij} is 1% of the absolute value of these impedances. The standard deviation of the estimated conductivities was computed using (12). We obtained that the uncertainty is 0.7% of the estimated conductivity for healthy tissue and 13.5% of the estimated conductivity for tumor. Uncertainty about tumor conductivity is greater because the tumor is small and located in the center of the system: the measurement system using the neighboring method is more sensitive in areas close to the electrodes, as shown in [19, 20].

TABLE III
RELATIVE VARIATION $\Delta Z_{ij}^{0}/Z_{ij}$ OF THE COMPUTED IMPEDANCES FOR THE NEIGHBORING METHOD, WITH AND WITHOUT THE TUMOR. $\sigma_{tumor} = 2.0\ \sigma_{tissue}$.

i-j	$\Delta Z_{ij}^{0}/Z_{ij}$	*i-j*	$\Delta Z_{ij}^{0}/Z_{ij}$
1-3	1.0 %	2-6	3.6 %
1-4	1.8 %	3-5	0.8 %
1-5	4.7 %	3-6	4.6 %
2-4	0.1 %	4-6	3.4 %
2-5	3.3 %		

B. *Clinical case*

We applied our method to estimate retrospectively tissue conductivity from the data collected during a clinical IRE trial, performed at the University Hospital of Poitiers. The patient was affected by a neuroendocrine tumor in the pancreas head and the IRE treatment was carried out using the Nanoknife device with three electrodes [29].

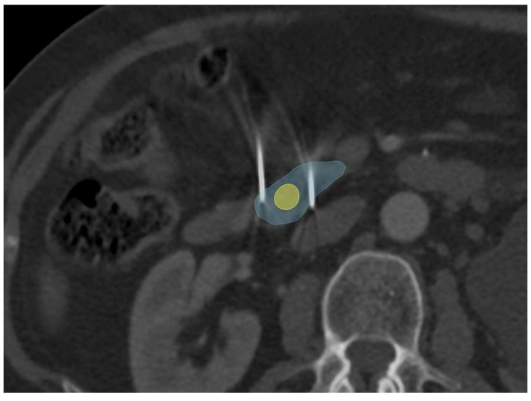

Fig. 2. Per-operative CT scan showing 2 of the 3 electrode tips with segmentation of the pancreas (blue) and tumor (yellow) superimposed on the CT image

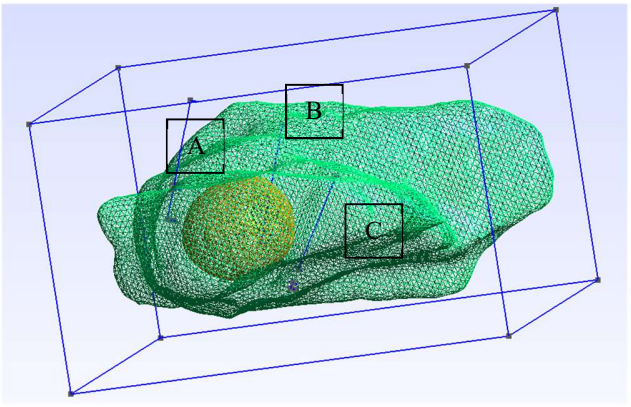

Fig. 3. Finite element mesh built with Gmsh. The CT segmentation of the pancreas surface is colored green; that of the tumor is colored orange. The three needles are in blue; note that needle A is divided into two parts, one inside the pancreas and the other inside the fictitious box that models the fat.

A pre-operative Computed Tomography (CT) scan with contrast was performed at the beginning of the IRE procedure to localize the target tumor. Next, the three needles were inserted percutaneously under CT guidance by the interventional radiologist, as parallel as possible around the tumor, and a CT scan was performed to check needle positioning (see Figure 2).

Manual segmentation of the pancreas gland and tumor was performed with 3D-Slicer [30] from the pre-operative CT scan, after non rigid registration had been applied using the per-operative CT scan (with the needles) as a reference. The coordinates of the three needles were collected by manual marking on the per-operative scan. These data were then imported into Gmsh [31] in order to build a finite element mesh (see Figure 3). A fictitious box was added to account for the fact that the pancreas is surrounded by fat; this box is parallelepipedic in shape to simplify the model. The 3D mesh was composed of 676 730 elements (see supplementary files 2).

As there were three needles (A, B and C) in this clinical trial, three electrode pairs were defined: A-B (pair #1), A-C (pair #2) and B-C (pair #3). The IRE treatment consisted here in applying, for each electrode pair, about eighty 90 µs pulses with an equivalent electric field (defined as the voltage divided by the distance between electrodes) of 1600 V/cm.

Prior to the IRE pulses, the Nanoknife generates a 400 V pre-pulse between the different electrode pairs successively. In parallel, the device measures voltage and current at the end of the pulse, when the steady-state assumption is best verified (see supplementary file 3). We used these data to compute the self-impedances: we found $Z_{11} = Z_{22} = 281.2\ \Omega$ and $Z_{33} = 202.4\ \Omega$.

When we observe the geometric model (Figure 3), we can see that the three electrodes are roughly equidistant from each other. If there were only one tissue, we would expect to measure three very close impedances. But electrode A is not completely inserted into the pancreas, unlike the other two electrodes B and C: part of electrode A is in the fat surrounding the pancreas. When this electrode is active, it is more difficult for the current to flow because fat is a poor conductor (compared to the pancreas). The impedance observed in this case will therefore be high. On the other hand, when electrode pair B-C is active, the current can flow in the pancreas without passing through the fat: the impedance observed in this case will therefore be low. This is why Z_{11} (electrode pair A-B is active) and Z_{22} (electrode pair A-C is active) are high compared to Z_{33} (electrode pair B-C is active).

In addition, as the electrodes are approximately equidistant, Z_{11} and Z_{22} should be close to each other, but not exactly equal as observed experimentally. This result is due to a measurement error. We analyzed the data files provided by the Nanoknife (see supplementary file 3) and found that the current (respectively the voltage) is recorded for IRE pulses with a resolution $\Delta I = 0.1$ A (respectively $\Delta V = 7$ V). Under these conditions, the relative error on the measured impedance $\Delta Z/Z$ ($= \Delta V/V + \Delta I/I$) is 6.2%.

On the other hand, as the distance between the electrodes is approximatively 1.7 cm, the pre-pulses induce an equivalent electric field of about 240 V/cm: the tissue electroporation threshold is a priori not reached (to be sure we should work with an even lower voltage but the Nanoknife does not allow to adjust it). Furthermore, we assume that there is no voltage drop at the electrode/tissue interface when a 400 V pulse is applied (see appendix for more details). From these considerations, we deduce that the impedances are only related to the electrical properties of non-electroporated tissues.

We therefore have three measurements to estimate the electrical conductivity of three tissues (pancreas, tumor and fat). The problem seems well posed. However, when we solved this problem by applying Algorithm I, we observed that it did not converge, particularly with regard to tumor conductivity. This result is due to the measurement errors mentioned above. To solve this issue, we modified the minimization problem (8) by adding a penalty term:

$$P([\boldsymbol{\Delta\sigma}]) = \|\boldsymbol{\sigma_0} - (\boldsymbol{\sigma} + \boldsymbol{\Delta\sigma})\|^2 \tag{14}$$

where $\boldsymbol{\sigma_0} = [\sigma_{0\ pancreas}, \sigma_{0\ tumor}, \sigma_{0\ fat}]$ is the expected conductivity of the different tissues and $\boldsymbol{\sigma} = [\sigma_{pancreas}, \sigma_{tumor}, \sigma_{fat}]$ the estimated conductivity at a given iteration of the algorithm.

We used the database [14] to set the expected conductivity $\sigma_{0\ pancreas} = 0.5$ S/m and $\sigma_{0\ fat} = 0.05$ S/m for pancreas and fat. As for $\sigma_{0\ tumor}$, to our knowledge, no data are available in the literature for neuroendocrine tumors, which are rare. On the other hand, there are studies in the literature for other tumor types. For a liver adenocarcinoma, low frequency conductivity was measured at 0.4 S/m in [32]. For human pancreatic tumors, a study was carried out with Patient-Derived Xenograft models in [33] and a conductivity of 0.2 S/m was observed at low electric field. In the following simulations, we chose 0.3 S/m for tumor conductivity.

With the penalty term (14), the solution is sought in a neighborhood of expected conductivities. The weight of this penalty term in (8), with respect to the impedance error term $\|[\boldsymbol{\Delta Z}] - [\boldsymbol{S}]\,[\boldsymbol{\Delta\sigma}]\|^2$, is controlled by the parameter α.

This parameter is set by considering, on the one hand, the error on the impedances $Z_{ii\ algo}$ computed by the algorithm:

$$\Delta Z/Z_{algo} = \max_{i=1,2,3}\left(|Z_{ii} - Z_{ii\ algo}|/Z_{ii}\right) \tag{15}$$

and, on the other hand, the uncertainty error on the estimated conductivities.

For the uncertainty analysis, we set the standard deviation ($\sqrt{VAR}$) for the different impedance measurements Z_{ii} according to the measurement accuracy, i.e. 6.2% of the absolute value of these impedances. The standard deviation of the conductivities was computed using (12).

Table IV reports the results for different values of α. The algorithm converges to a non-physical solution (tumor conductivity is negative) when $\alpha = 10$. For $\alpha = 100$, the algorithm converges after 3 iterations to a physical solution with an error $\Delta Z/Z_{algo}$ equal to 0.5%, which is small in front of the measurement error $\Delta Z/Z$ (6.2%). However, uncertainty about the value of tumor conductivity is very high (± 0.866 S/m). For $\alpha = 1000$, this uncertainty decreases but remains significant (± 0.133 S/m). For $\alpha = 10^4$, this uncertainty is much smaller (± 0.014 S/m), while the error $\Delta Z/Z_{algo}$ remains low (2.2 %). For $\alpha = 10^5$, the error on $\Delta Z/Z_{algo}$ increases significantly to 9.9%.

TABLE IV
NUMERICAL STUDY FOR THE CLINICAL CASE.

α	10	100	1000	10^4	10^5
$\Delta Z/Z_{algo}$ (%)	No physical solution	0.5	0.9	2.2	9.9
$\sigma_{pancreas}$ (S/m)	×	0.382 ± 0.084	0.371 ± 0.044	0.383 ± 0.038	0.445 ± 0.016
σ_{tumor} (S/m)	×	0.092 ± 0.866	0.263 ± 0.133	0.290 ± 0.014	0.295 ± 0.002
σ_{fat} (S/m)	×	0.083 ± 0.053	0.076 ± 0.033	0.066 ± 0.029	0.030 ± 0.013

We retained the results for $\alpha = 10^4$. It is worth noting that if the measurement uncertainty had been lower, the weight of the penalty term would have been lower.

The final value of the estimated conductivity is 0.383 ± 0.038 S/m for pancreas, 0.290 ± 0.014 S/m for tumor and 0.066 ± 0.029 S/m for fat. The uncertainty error for the pancreas and tumor is less than the inter-individual variability observed on traditional bioimpedance measurements for healthy tissue [13] and tumors [32]. However, the uncertainty error for fat is slightly higher than the one given in [13].

To improve system accuracy, the resolution of voltage/current measurements should be refined in clinical devices. In addition, the estimate would be more accurate if a larger number of measurements were available. The Nanoknife can only measure self-impedances (i.e. Z_{ii}). If it were possible to access mutual impedances (i.e. Z_{ij} with $i \neq j$), the accuracy of the system would be significantly improved. In the case of a 3-electrode system, we would have six independent measurements (taking into account reciprocity) compared with three in the study presented in this article.

Another limitation of the work presented is that the conductivity estimation provided at this stage is not sufficient to calibrate electroporation models. As mentioned in the introduction, these models are nonlinear and the dependence of conductivity on electric field is characterized by two DC conductivity values: one at low electric field and one at high electric field [10]. The conductivity estimation presented here provides information at low electric field. The DC conductivity at high electric field can be extracted by estimating high-frequency conductivity at low electric field (in both cases, the cell membrane no longer acts as an insulator). High-frequency impedance measurements with small signals (typically a few mA at frequencies of a few hundred kHz, commonly applied in EIT [19]) using the same electrodes would therefore be necessary to characterize DC conductivity at high electric field. The method described in this article could then be implemented with high-frequency data. Unfortunately, clinical IRE devices do not yet allow this type of measurement.

IV. Conclusion

In this article, we investigated the possibility of exploiting imaging and voltage/current measurements, made prior to IRE treatment, with needles inserted near a deep-seated tumor. The conductivity of the different tissues can be estimated in the tumor vicinity, using an approach similar to that developed for EIT. However, imaging is essential to build a specific geometric model and compensate for the lack of information resulting from the small number of electrodes available.

Numerical simulations in a 3D canonical case with six electrodes show the relevance of this approach: the algorithm converges very quickly, in a few iterations. A clinical case study with real data confirms the feasibility of the proposed method.

This approach also makes it possible to quantify the uncertainty in the estimation of tissue conductivity as a function of measurement error. In the clinical case discussed in this article and depending on the tissue considered, the uncertainty error is

lower than, or of the same order of magnitude as, that found in the literature, where the precision of results is limited by the variability between individuals. However, the results obtained in this paper are limited by the performance of current clinical devices. The results could be improved in a number of ways, for example by measuring voltage/current with greater resolution, by performing voltage measurements on inactive electrodes to provide more information, or by working with low-amplitude high-frequency signals to refine electroporation models.

As it stands, the method proposed in this article can be used to expand knowledge on tumors. The literature shows important variations in the tumor conductivity values according to the type of tumors, their origin (primary versus metastatic) and their content in terms of necrosis or fibrosis. We are currently working on this issue by combining the analysis of impedance measurements and imaging on a database of patients treated by IRE for hepatic and pancreatic tumors.

APPENDIX

When a DC current flows across an electrode, there is a charge transfer resistance R_{CT} due to Faradic processes at the electrode/electrolyte interface. This resistance is nonlinear with respect to the overpotential η [34]:

$$R_{CT}(\eta) = \frac{\eta}{I_0}\left(e^{\alpha_a \frac{nF}{RT}\eta} - e^{-\alpha_c \frac{nF}{RT}\eta}\right)^{-1} \tag{16}$$

where R is the gas constant, T is the temperature in Kelvin, F is Faraday's constant, n is the number of electrons per molecule participating in the reaction, I_0 is the exchange current (in A), α_a and α_c are the transfer coefficients.

The higher the applied voltage, the higher the Faradic current, resulting in an increasingly low voltage drop at the electrode/electrolyte interface. To illustrate this statement, we propose to compute the numerical value of R_{CT} using the parameters reported in [34] for a platinum/electrolyte interface: $I_{0\,norm} = 6.41\ 10^{-4}$ Am^{-2}, $n = 2$, $\alpha_a = \alpha_c = 0.5$ and $T = 298$ K. $I_{0\,norm}$ is the normalized value of I_0 obtained for 1 m² electrode surface. Here we use the surface of a real needle, with an active length of 40 mm and a diameter of 1 mm, to compute I_0. When the overpotential is small (i.e. $\eta << RT/F = 25$ mV), R_{CT} is very large and nearly constant (≈ 150 kΩ). When the overpotential is large (i.e. $\eta >> 25$ mV), R_{CT} becomes negligible ($5.2\ 10^{-11}$ Ω for $\eta = 1$ V)

Signals used in EIT are small (currents are limited to 0.1 mA in the low frequency range [19]). Under these conditions, R_{CT} resistance has a strong influence on impedance measurements using an electrode where the current flows.

For impedance measurements with an IRE device, we use pre-pulses of about 400 V. Under these conditions, R_{CT} resistance is almost zero and impedance measurements reflect only the tissue response, even when using an electrode where the current flows.

To confirm this theoretical result, we measured the potato conductivity σ_{potato} using four electrodes as shown in Figure 4. The system was scanned with the same tools as those presented in section III.B, in order to build an accurate finite element model of the potato with the exact position of the electrodes. In addition, we verified with imaging that the plant tissue was visibly homogeneous, implying that conductivity can be considered constant at any point of the potato.

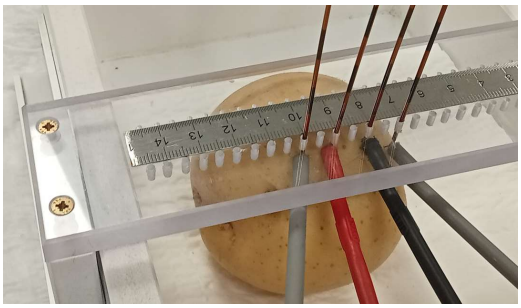

Fig. 4. Experiment with a potato and 4 electrodes.

A first measurement was performed with the 2-electrode system using only pair #1 of external electrodes and a second measurement with the 4-electrode system using all the electrodes (pair #1 of external electrodes and pair #2 of inner electrodes).

For measurement with the 2-electrode system, a current I_1 was injected into one electrode of pair #1 and collected in the other electrode of pair #1. At the same time, the voltage ΔV_{11} was measured between the electrodes of pair #1. The impedance $Z_{11} = \Delta V_{11}/I_1$ was computed according to (1).

For measurement with the 4-electrode system, the voltage ΔV_{21} was measured between the electrodes of pair #2 while the current I_1 described previously flowed. The impedance $Z_{21} = \Delta V_{21}/I_1$ was computed according to (1).

From a practical point of view, we used a low voltage generator to apply $\Delta V = \Delta V_{11} = 20.0$ V for about 200 ms. We used a Chauvin Arnoux DP25 probe (respectively Chauvin Arnoux E3N probe) to measure voltage (respectively current) and an oscilloscope for signal acquisition. At the end of the pulse, we measured $\Delta V_{21} = 4.24$ V and $I_1 = 40$ mA. The 20 V voltage was

chosen to be high enough to work in the high voltage range (>> 25 mV) but also to ensure that the current signal comes out of the noise (> 10 mA, 4 turns were made around the current clamp to amplify the current measurement). On the other hand, it was not possible to work with a higher voltage or a longer pulse because of the potato electrolysis, which ends up modifying the ionic concentration (and therefore the conductivity). These changes would result in a gradual increase in current over the duration of the pulse.

For the numerical computation, we solved problem (3) for $m = 1, 2$ in the case of a reference conductivity equal to 1 S/m. We used (2) to compute the unit impedances $Z_{11\ unit}$ and $Z_{21\ unit}$, which are rigorously equal to the inverse of probe cell constant defined in impedance measurements [35]. We found $Z_{11\ unit} = 40.25\ m^{-1}$ and $Z_{21\ unit} = 8.31\ m^{-1}$.

Then, the potato conductivity was extracted by calculating $\sigma_{potato\ 2} = Z_{11\ unit} / Z_{11} = 0.0201$ S/m for the 2-electrode system and $\sigma_{potato\ 4} = Z_{21\ unit} / Z_{21} = 0.0196$ S/m for the 4-electrode system. These conductivities are within the order of magnitude expected for potato tissue (0.04 S/m in [36]). Above all, they are very close (relative deviation of 2.5 %), confirming that there is no effect of the charge transfer resistance at high voltages. Otherwise, this effect would only have affected the measured impedance Z_{11} but not Z_{21}; the conductivity value $\sigma_{potato\ 2}$ would have been much lower than $\sigma_{potato\ 4}$.

ACKNOWLEDGMENT

This research has been partly granted by the Plan Cancer project MECI n◦21CM119-00 led by C. Poignard. The Bernoulli lab supports O. Sutter and C. Poignard through the projects NEPA and EVALHEP.

REFERENCES

[1] O. Sutter et al., "Safety and Efficacy of Irreversible Electroporation for the Treatment of Hepatocellular Carcinoma Not Amenable to Thermal Ablation Techniques: A Retrospective Single-Center Case Series," *Radiology*, vol. 284, no. 3, pp. 877-886, 2017

[2] D. Miklavcic and R. V. Davalos, "Electrochemotherapy (ECT) and irreversible electroporation (IRE)-advanced techniques for treating deep-seated tumors based on electroporation," *Biomedical Engineering online*, vol. 14, no. 3, pp. 1-7, 2015

[3] L. G. Campana et al., "Electrochemotherapy–Emerging applications technical advances, new indications, combined approaches, and multi-institutional collaboration," *European Journal of Surgical Oncology*, vol. 45, no. 2, pp. 92-102, 2019

[4] A. H. Ruarus et al., "Percutaneous irreversible electroporation in locally advanced and recurrent pancreatic cancer (PANFIRE-2): a multicenter, prospective, single-arm, phase II study," *Radiology*, vol. 294, no. 1, pp. 212-220, 2020

[5] M. Meijerik et al, "Irreversible Electroporation to Treat Unresectable Colorectal Liver Metastases (COLDFIRE-2): A Phase II, Two-Center, Single-Arm Clinical Trial," *Radiology*, vol. 299, no. 2, 2021

[6] R. E. Neal, P. A. Garcia, J. L. Robertson and R. V. Davalos, "Experimental Characterization and Numerical Modeling of Tissue Electrical Conductivity during Pulsed Electric Fields for Irreversible Electroporation Treatment Planning," *IEEE Trans. Biomedical Engineering*, vol. 59, no. 4, pp. 1076–1085, 2012.

[7] A. Zupanic, B. Kos and D. Miklavcic, "Treatment planning of electroporation-based medical interventions: electrochemotherapy, gene electrotransfer and irreversible electroporation," *Physics in Medicine and Biology*, vol. 57, no. 17, pp. 5425–5440, 2012.

[8] O. Sutter, A. Fihri, R. Ourabia-Belkacem, N. Sellier, A. Diallo, and O. Seror, "Real-time 3d virtual target fluoroscopic display for challenging hepatocellular carcinoma ablations using cone beam CT," *Technology in Cancer Research & Treatment*, vol. 17, 2018

[9] O. Gallinato, B. Denis de Senneville, O. Seror and C. Poignard, "Numerical workflow of irreversible electroporation for deep-seated tumor," *Physics in Medecine and Biology*, vol. 64, no. 5, 2019

[10] O. Gallinato et al. "Numerical modelling challenges for clinical electroporation ablation technique of liver tumors," *Mathematical Modelling of Natural Phenomena,* vol. 15, no. 11, 2020

[11] D. Sel, D. Cukjati, D. Batiuskaite, T. Slivnik, L.M. Mir and D. Miklavcic, "Sequential finite element model of tissue electropermeabilization," *IEEE Trans. Biomedical Engineering*, vol. 52, no 5, pp. 816–827, 2005.

[12] M. Breton et al, "Non-Linear Steady-State Electrical Current Modeling for the Electropermeabilization of Biological Tissue," *IEEE Trans. Magnetics*, vol. 51, no. 3, 2015

[13] C Gabriel, A Peyman and E. H. Grant, "Electrical conductivity of tissue at frequencies below 1 MHz," *Physics in Medecine and Biology*, vol. 54, pp. 4863–4878, 2009

[14] C. Gabriel, S. Gabriel, and E. Corthout, “The dielectric properties of biological tissues: I. literature survey,” *Physics in Medicine and Biology*, vol. 41, pp. 2231-2249, 1996

[15] J. K. Seo et al., “Electrical tissue property imaging using MRI at dc and Larmor frequency,” *Inverse Problems*, vol. 28, no. 8, 2012.

[16] A. Ivorra, B. Al-Sakere, B. Rubinsky and L. M. Mir, “In vivo electrical conductivity measurements during and after tumor electroporation: conductivity changes reflect the treatment outcome,” *Physics in Medecine and Biology*, vol. 54, pp. 5949–5963, 2009

[17] Zhao Y et al, “Ablation outcome of irreversible electroporation on potato monitored by impedance spectrum under multi-electrode system”, *Bio-Medical Engineering OnLine*, vol. 17, no. 1, 2018

[18] R. V. Davalos, D. M. Otten, L. M. Mir and B. Rubinsky, “Electrical Impedance Tomography for Imaging Tissue Electroporation,” *IEEE Trans. Biomedical Engineering*, vol. 51, no. 5, 2004

[19] A. Adler and A. Boyle, “Electrical Impedance Tomography: Tissue Properties to Image Measures,” *IEEE Trans. Biomedical Engineering*, vol. 64, no 11, 2017

[20] P. Kauppinen, J. Hyttinen, and J. Malmivuo, “Sensitivity Distribution Visualizations of Impedance Tomography Measurement Strategies,” *International Journal of Bioelectromagnetism, v*ol. 8, no. 1, pp. 63-71, 2006

[21] Yang Y., Jia, J., Smith S., Jamil N., Gamal W. and Bagnaninchi P. O., “A miniature electrical impedance tomography sensor and 3-D image reconstruction for cell imaging,” *IEEE Sensors Journal*, vol. 17, no. 2, pp. 514-523, 2016

[22] D. B. Geselowitz, “An application of electrocardiographic lead theory to impedance plethysmography,” *IEEE Trans. Biomedical Engineering*, vol. 18, pp. 38-41, 1971.

[23] T. Murai and Y. Kagawa, “Electrical Impedance Computed Tomography Based on a Finite Element Model,” *IEEE Trans. Biomedical Engineering*, vol. 32, no. 3, 1985

[24] M. Vauhkonen, D. Vadasz, P. A. Karjalainen, E. Somersalo and J. P. Kaipio, “Tikhonov Regularization and Prior Information in Electrical Impedance Tomography,” *IEEE Trans. Medical Imaging*, vol. 17, no. 2, 1998.

[25] J. M. Bioucas-Dias and M. A. T. Figueiredo, “A New TwIST: Two-Step Iterative Shrinkage/Thresholding Algorithms for Image Restoration,” *IEEE Trans. Image Processing*, vol. 16, no. 12, 2007

[26] https://freefem.org/

[27] Andrea Borsic et al, “*In Vivo* impedance imaging with total variation regularization”, *IEEE Trans. on Medical Imaging*, vol. 29, no. 1, 2010

[28] P. C. Hansen, “Discrete inverse problems: insight and algorithms”, *Society for Industrial and Applied Mathematics*, chap. 7, 2010.

[29] J.-P. Tasu, M. Vionnet, L. Laffite and C. Poignard, “Percutaneous irreversible electroporation for the treatment of pancreatic insulinoma,” *Diagnotic and Interventional Imaging*, vol. 104, no. 6, pp. 307-308, 2023.

[30] A. Fedorov et al, “Percutaneous irreversible electroporation for the treatment of pancreas insulinoma,” *Magnetic Resonance Imaging*, vol. 30, no. 9, pp. 1323-1341, 2012

[31] C. Geuzaine and J.-F. Remacle. “Gmsh: a three-dimensional finite element mesh generator with built-in pre- and post-processing facilities,” *International Journal for Numerical Methods in Engineering*, vol. 79, no. 11, pp. 1309-1331, 2009.

[32] D. Haemmerich, D.J. Schutt, A.W. Wright, J.G. Webster and D.M. Mahvi, ″Electrical conductivity measurement of excised human metastatic liver tumours before and after thermal ablation*″, Physiological Measurement*, vol. 30, pp. 459-466, 2009

[33] R. M. Brock, N. Beitel-White, S. Coutermarsh-Ott, D. J. Grider, M. F. Lorenzo, V. M. Ringel-Scaia and Navid Manuchehrabadi, ″Patient Derived Xenografts Expand Human Primary Pancreatic Tumor Tissue Availability for ex vivo Irreversible Electroporation Testing*″, Frontiers in Oncology,* Sec. Cancer Molecular Targets and Therapeutics, vol. 10, 2020

[34] D. R. Cantrell, S. Inayat, A. Taflove, R. S. Ruoff and J. B Troy, “Incorporation of the electrode–electrolyte interface into finite-element models of metal microelectrodes,” *Journal of Neural Engineering*, vol. 5, no. 1, pp. 54–67, 2008

[35] A. Ivorra and B. Rubinsky, “In vivo electrical impedance measurements during and after electroporation of rat liver,” *Bioelectrochemistry*, vol. 70, no. 2, pp. 287–295, 2007.

[36] A. Silve, “Nouveaux dispositifs pour l’application contrôlée d’impulsions électriques nanosecondes et pour la détection de leurs effets sur les cellules”, Ph. D. dissertation, University of Paris 11, pp. 79-81, 2011